

Hybrid Spinel Iron Oxide Nanoarchitecture Combining Crystalline and Amorphous Parent Material

Sawssen Slimani, Giorgio Concas, Francesco Congiu, Gianni Barucca, Nader Yaacoub, Alessandro Talone, Mourad Smari, Essebti Dhahri, Davide Peddis, and Giuseppe Muscas*

Cite This: *J. Phys. Chem. C* 2021, 125, 10611–10620

Read Online

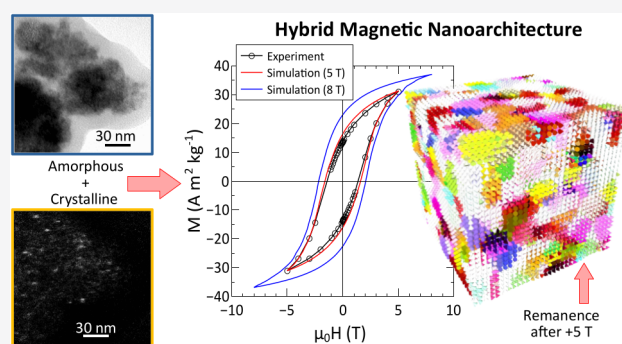
ACCESS |

Metrics & More

Article Recommendations

Supporting Information

ABSTRACT: When preparing nanostructured magnetic materials, the presence of an amorphous component is often considered a weakness of the synthesis method and a waste of material. This stems because the amorphous fraction is often pictured as a “dead” magnetic component, showing little to no contribution to the magnetic properties, for example, saturation magnetization. For this reason, additional steps are employed after the main synthesis process to reduce or isolate and remove the amorphous phase from the “optimal” crystalline product. Here, we propose a hybrid-structured nanoarchitecture that combines crystalline cobalt ferrite and the amorphous parent material. The latter contributes partially to the total magnetic moment but exhibits a magnetic anisotropy much larger than the crystalline bulk parent material. With the information obtained from an in-depth structural and magnetic characterization, a micromagnetic model is created, allowing identifying the contribution of each component elucidating the active role of the amorphous phase. The extremely low cost, minimal complexity, and high yield of the synthesis process make this hybrid design of large interest for technological applications.



INTRODUCTION

Magnetic nanostructured systems represent a class of materials with large application potential thanks to their unique physical properties. Reducing magnetic systems down to the nanoscale makes the multidomain organization energetically unfavorable, hence promoting the formation of magnetic single-domain particles, where all atomic spins act as a single magnetic “supermoment”.¹ In this framework, designing magnetic nanostructures means controlling their physical behavior and tailoring their magnetic properties for individual technological applications. Indeed, the peculiar properties of nanostructured materials based on monodomain nanoparticles (NPs) are appealing for a multitude of technological fields, such as nanomedicine² (e.g., magnetic sensors,³ bioimaging,^{4,5} drug delivery,⁶ therapeutic hyperthermia^{7–10}), ferrofluid technology,¹¹ catalysts,¹² color imaging,¹³ high-density magneto recording,¹⁴ and recently they have found an important role in thermoelectric systems.^{15–17}

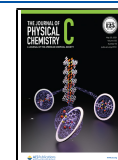
The presence of an amorphous phase in nanostructured magnetic materials is traditionally considered a negative side effect of the synthesis method. Indeed the amorphous fraction is often depicted as a “dead” magnetic component, and hence as a waste of material, due to its typical scarce contribution to the effective saturation magnetization. For the simplest case of magnetic nanoparticles, this picture is usually described by the core/shell morphology with an ordered core and a shell with

structural/magnetic disorder.^{18–21} This aspect is even more important for bimagnetic nanoarchitectures (e.g., core–shell bimagnetic structure, particles embedded in a magnetic matrix) since ordered interfaces are fundamental to maximize the coupling among the individual components.²² However, interfaces are difficult to control, in particular, due to the defects associated with crystalline interfaces such as dislocation and grain boundaries.²³ On the other hand, fully amorphous composite materials, thanks to the continuous homogeneous disordered structure, do not show conventional sharp interfaces, opening the way to exotic long-range properties.²⁴ Despite the apparent duality between crystalline and amorphous systems, one should consider this picture like a continuum. For instance, the topological properties induced by local defects in crystalline structures represent an additional degree of freedom in tuning the properties of the material.²⁵ A typical example is the enhanced magnetic anisotropy due to defects/distortions at nanoscale interfaces.²⁶ However, a

Received: January 28, 2021

Revised: April 24, 2021

Published: May 11, 2021



rational correlation between defects and magnetic properties is still lacking in the literature.

Spinel iron oxides are one of the most versatile materials to engineer magnetic nanostructures with tunable properties.^{27–30} Such systems can be efficiently prepared by wet chemical methods,^{31–36} in particular, coprecipitation is widely employed to synthesize spinel iron oxide nanoparticles due to its simplicity, use of safe reagents, and high yielding.^{34,37} This technique entails the reaction of a metal salt with a base in an aqueous solution to form metal oxides.^{38–40} Typically, the reaction proceeds in two steps: hydrolysis (i.e., formation of metal cations oxo, hydroxo complexes) and hydroxylation (i.e., condensation of metal cations oxo, hydroxo complexes).^{41–44} The hydroxylation rate is a function of the pH of the medium and controls the type and the structure of the condensed species. Therefore, in low-temperature coprecipitation processes, the pH of the solution represents a useful tool to control the growth of ultrafine particles and the ratio between crystalline and amorphous phase.⁴⁵

Here, we investigate the magnetic properties of a hybrid nanoarchitecture combining crystalline cobalt ferrite and the amorphous parent material. The latter contributes partially to the total magnetic moment but exhibits a very large magnetic anisotropy. Crosschecking the information obtained from structural and magnetic characterization, a micromagnetic model is proposed. This model sheds light on the contribution of each component elucidating the active role of the amorphous phase and permitting an understanding of the general properties of this unconventional hybrid crystalline–amorphous nanostructure.

EXPERIMENTAL AND COMPUTATIONAL METHODS

Synthesis. In a typical synthesis, 100 mL of HCl solution was loaded into 2-necked glass flask, one of which connected to a vacuum and a gas inflow port, and the other used for the materials' transfer. The balloon was submerged in a water bath and the solution was heated to 60 °C under stirring at 630 rpm. The solution was purified alternating between vacuum and nitrogen (N₂) gas three times. The N₂ flow remained, and a mixture of 3.15 mmol CoCl₂·4H₂O and 6.21 mmol FeCl₃·6H₂O was added to the balloon. After mixing for 60 min, 20 mL of ammonium hydroxide (30%), previously deoxygenated (10 min under N₂ reflux), was added, leading to an abrupt transition from pH = 2–9.5, accompanied by the solution visually turning to a reddish-brown color. After 60 min, the magnetic nanoparticles were collected using a centrifuge and washed for five cycles with distilled water (15 min, 6000 rpm). Finally, the magnetic nanoparticles were dried at 60 °C overnight.

Experimental Techniques. Phase identification was carried out by X-ray powder diffraction (XRD), using Seifert TT 3003 diffractometer equipped with secondary graphite monochromator using Cu–K_α radiation. The measurement was performed in the 2θ range 10°–70° with a step size of 0.04° and counting time 4 s per step.

The morphology of the sample was investigated by transmission electron microscopy (TEM) technique by using a Philips CM200 electron microscope operating at 200 kV and equipped with a LaB₆ filament. For TEM observations, the powdered samples were dispersed in ethanol and submitted to ultrasound agitation for approximately 1 min. A drop of the suspension was deposited over a commercial TEM grid,

covered with a thin holey carbon film, and kept in the air at room temperature until complete ethanol evaporation. The particle size distribution was calculated by analyzing the TEM images with the ImageJ software⁴⁶ and fitting a log-normal function to the frequency count of the particles' size.

Mössbauer spectra were recorded in transmission geometry using a ⁵⁷Co/Rh γ-ray source mounted on an electromagnetic driving unit submitted to a triangular velocity form. The experiments were carried out at 12 K using a bath cryostat. The quantity of powder was optimized at about 5 mg of Fe/cm². The fitting procedure was done using the homemade unpublished MOSFIT software involving magnetic sextets and quadrupolar components with Lorentzian lines.

DC magnetization measurements were performed using a superconducting quantum interference device (SQUID) magnetometer. The sample, in the form of powder, was fixed in a capsule, to prevent any movement of the nanoparticles during the measurements, and all the magnetic measurements were normalized by the real mass of the measured sample. The saturation magnetization *M*_s was extrapolated by fitting the curves at high field using the Law of Approach to Saturation (LAS)⁴⁷

$$M = M_s \left(1 - \frac{A}{H} - \frac{B}{H^2} \right) \quad (1)$$

where *A* and *B* are constant parameters.

RESULTS AND DISCUSSION

Structural and Magnetic Properties. The XRD pattern (Figure 1) shows the reflections of a crystalline phase

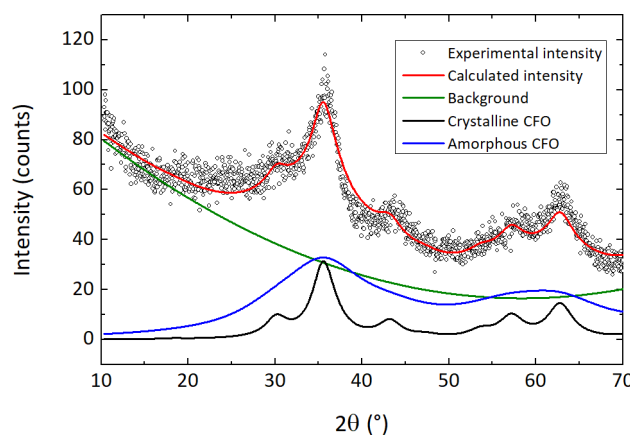


Figure 1. Experimental XRD pattern (black dots) and its Rietveld refinement (red line) using a crystalline cobalt ferrite component (black line) and a corresponding amorphous one (blue line). The calculated background intensity is reported as a green line.

corresponding to the fcc structure of the precipitated cobalt ferrite in pH = 9.5 (database code ICSD 257981). However, the presence of a wide hump compatible with a large amount of an amorphous phase is evident, which suggests the presence of small crystalline cobalt ferrite nanoparticles embedded within an amorphous parent material matrix. The obtained results agreed with the growth mechanism of cobalt ferrite particles in coprecipitation at the pH < 10, where some of the cobalt ions remain in the solution and form a non-stoichiometric hydroxide precipitate. On the other hand, for pH > 10, the solution leads to the formation and conversion of

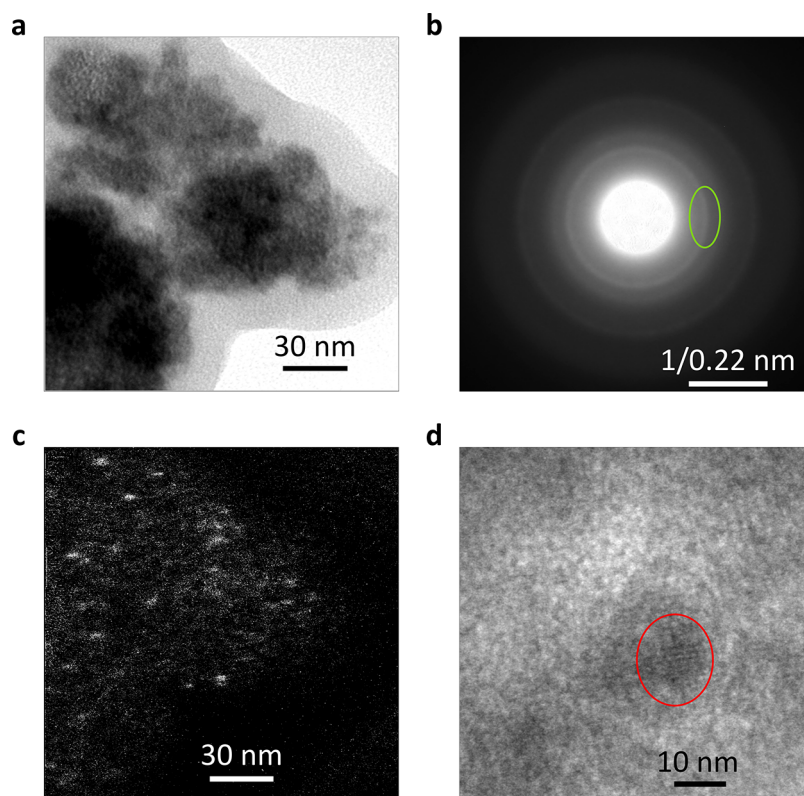


Figure 2. (a) Bright-field TEM image showing the powdered sample composed of primary aggregates (~ 100 nm) having a granular structure. (b) Corresponding selected area electron diffraction pattern. The diffuse intensity of the diffraction rings suggests the presence of small crystals in an amorphous matrix. (c) Dark-field image obtained with the portion of the diffraction ring encircled in (b) revealing the presence of small crystalline nanoparticles (bright spots) uniformly dispersed in the amorphous granular matrix. (d) High-resolution TEM image showing the atomic planes of a crystalline nanoparticle inside the amorphous matrix.

Co(OH)_x^{2-x} species to Co(OH)_3^- species, which are more insoluble. Therefore, higher pH values are needed to precipitate cobalt ions.^{43,48} Moreover, as a way to confirm the role of pH on the final product, we proved that by reducing the percentage of Co^{2+} content to 25% in the starting mixture, the degree of crystallinity of the samples increases considerably (see Figure S1 and the corresponding section in Supporting Information).

TEM analysis confirms this picture. In particular, bright-field TEM observations show that the sample is composed of large aggregates (about 100 nm) having a granular structure (Figure 2a and Figure S2 in Supporting Information). Aggregates are poorly crystallized as revealed by selected area electron diffraction (SAED) measurements. Figure 2b shows the SAED pattern corresponding to the area of the sample visualized in Figure 2a. It is composed of diffraction rings having a diffuse intensity typical of a large number of small crystals randomly oriented and dispersed inside an amorphous matrix. The lattice distances associated with diffraction rings are ascribable to the presence of the fcc cobalt ferrite phase, in accordance with XRD measurements. In order to show the spatial distribution of the nanocrystals, dark-field TEM observations were performed. Figure 2c shows the dark-field image of Figure 2a obtained selecting the portion of the diffraction ring encircled in Figure 2b. The crystals responsible for those diffraction spots appear brighter in the image, and the presence of a fine and uniform dispersion of very small crystalline particles is evident. The crystalline/amorphous nature of the sample was further investigated by high-

resolution (HR) TEM analysis. A typical HR-TEM image of the sample is reported in Figure 2d. The major part of the sample shows a granular (orange peel) contrast usually ascribable to amorphous material, but in the encircled region the atomic planes of a small particle are clearly visible, confirming the dispersion of nanocrystals inside an amorphous matrix.

Applying the Debye–Scherrer formula to the most intense reflection of the XRD pattern peak provides an estimation of the average coherent crystalline domain of about 3 nm. This value is in line with what was visually observed in several TEM images. Moreover, this value is compatible within the relative experimental error with the Rietveld refinement of the XRD pattern, carried out with the software MAUD⁴⁹ (Figure 1). Assuming that the amorphous phase can be modeled with the same local structure of the crystalline one,⁵⁰ the sample was simulated as a two-phase system, a crystalline cobalt ferrite phase with standard bulk parameters, and an equivalent one where the starting value of grain size was manually adjusted to reproduce the amorphous humps visible under the crystalline peaks, which were not reproducible with a simple second order polynomial background. The refinement of the microstructure of the sample confirms the presence of regular crystalline grains of 3.4(5) nm representing about 25% of the total volume of the sample. The residual volume (75%) is occupied by the amorphous parent material having similar structure, but a very small granular size of 0.9(5) nm, responsible of the missing long-range order. Interestingly, both phases exhibit little to no microstrain, estimated in $0(5) \times 10^{-5}$ and $9(5) \times$

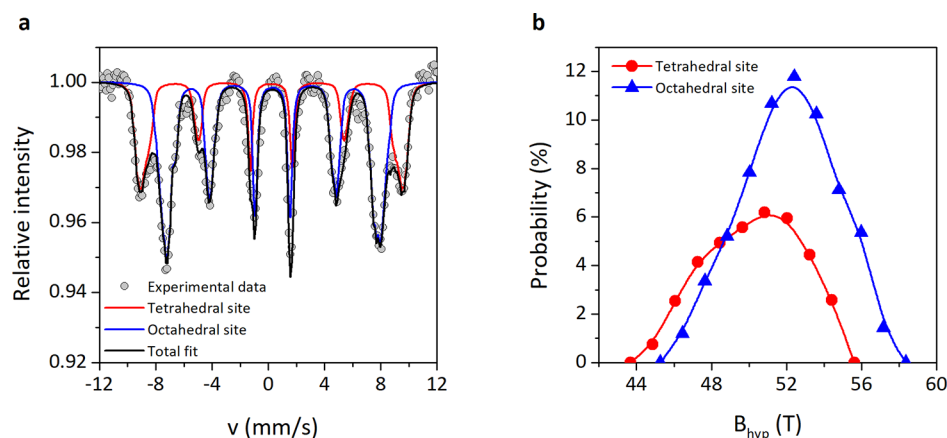


Figure 3. (a) Mössbauer spectrum recorded at 12 K with an applied field of 8 T. The spectrum is composed of a total sextet for iron in the tetrahedral position T_d (red line) and one for the octahedral position O_h (blue line). (b) Distribution of the hyperfine field (B_{hyp}) observed for both T_d and O_h sites obtained by the fitting procedure.

Table 1. Mean Values of the Hyperfine Parameters Extracted from the Fit to the Experimental Data^a

component	δ (mm s ⁻¹)	2ϵ (mm s ⁻¹)	B_{eff} (T)	θ_c (deg)	B_{hyp} (T)	%
T_d	0.41	0.01	57.0	37	50.8	36
O_h	0.49	0	46.8	51	52.2	64

^aIsomer shift (δ), quadrupole splitting (2ϵ), effective magnetic field (B_{eff}), average canting angle (θ_c), hyperfine field (B_{hyp}), and the % occupancy of each site.

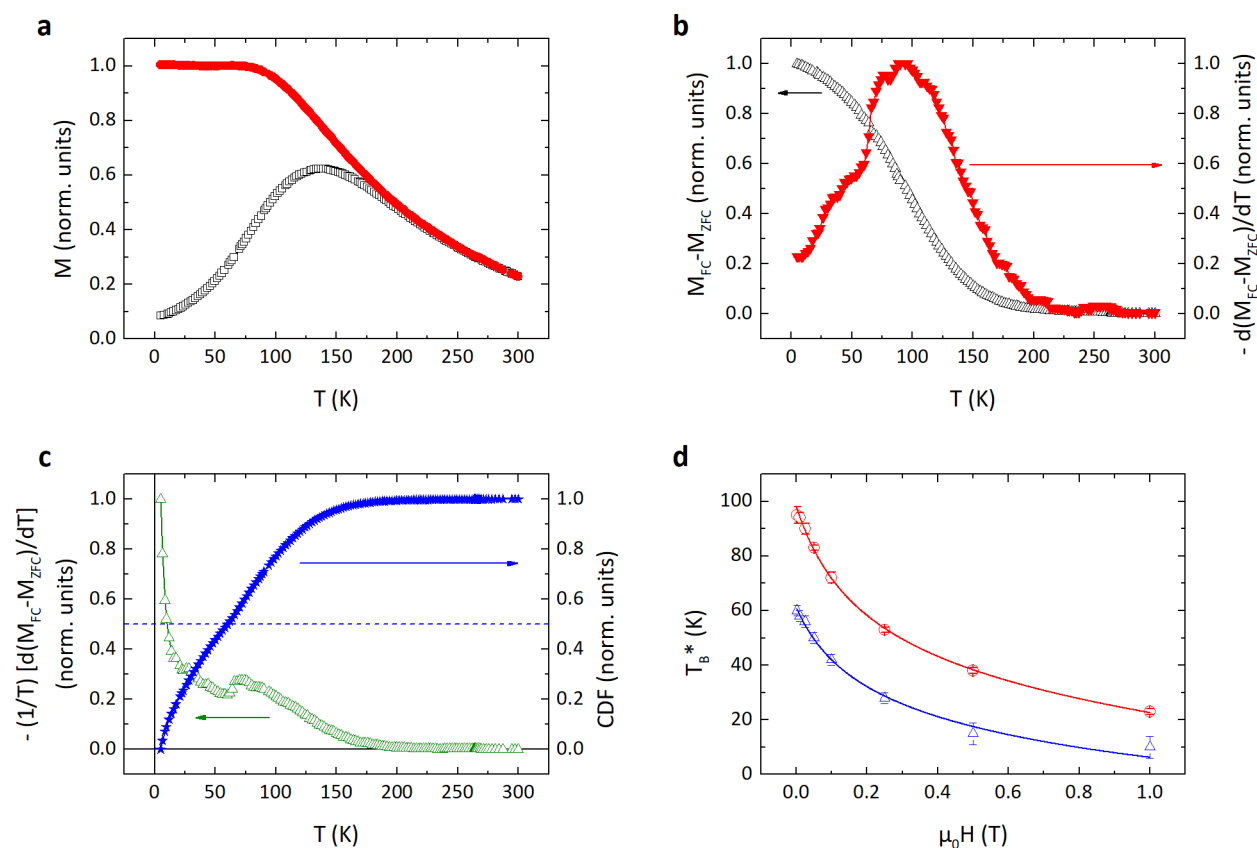


Figure 4. (a) ZFC (empty black squares) and FC (full red circles) curves measured with an applied field of 2.5 mT. (b) The corresponding FC–ZFC curve (empty black triangles) and the negative derivative representing the blocking temperature distribution (reversed full red triangles). (c) The corresponding $-1/T [d(M_{\text{FC}} - M_{\text{ZFC}})/dT]$ curve (empty green triangles) and its cumulative distribution function (CDF) (full blue stars). (d) Variation of the blocking temperature calculated with the conventional formulation (empty red circles) and the de Almeida formulation (empty blue triangles) as a function of the applied field with the corresponding fit of eq 4 to the experimental data (red and blue line, respectively).

10^{-5} for the crystalline and amorphous component, respectively.

The magnetic structure of the samples was studied by means of Mössbauer spectrometry under an intense magnetic field, allowing one to obtain information about the magnetic structure (see [Supporting Information](#) for additional details).^{51,52} The spectrum has been recorded at 12 K with a magnetic field of 8 T applied parallel to the γ -ray direction (Figure 3a). The intense applied magnetic field sums up with the hyperfine field of the tetrahedral (T_d) sites and opposes that of the octahedral (O_h) ones of the spinel structure, consistent with ferrimagnetic structure.^{53,54} Furthermore, with an external magnetic field parallel to the γ -ray direction, any Fe^{3+} magnetic moments noncollinear to the applied field will raise the intensity of the second and fifth lines of the sextet, otherwise equal to zero.^{54,55} The spectrum is characterized by broad asymmetrical lines indicating the presence of magnetically disordered structure with the clear signature of the presence of a large fraction of canted spins with a significant average canting angle for T_d and even more for O_h sites (Table 1). This complex magnetic structure is reproduced by a hyperfine field distribution (Figure 3b) correlated to a canting angle distribution.⁵⁶ Table 1 reports the mean values of the hyperfine parameters, attributed to Fe^{3+} in T_d and O_h sites,⁵⁶ hence confirming the presence of cobalt ferrite.

The thermal dependence of the magnetic properties of the sample was studied with the zero field-cooled (ZFC) and field-cooled (FC) curves reported in Figure 4a. The temperature corresponding to the maximum of the ZFC curve (T_{max}) is directly proportional to the average blocking temperature (T_B),⁵⁷ which in turn reflects the anisotropy energy barrier for the magnetization reversal. For noninteracting particles, the effective distribution of energy barriers is typically estimated as (Figure 4b)^{58,59}

$$f(T) \propto -\frac{d(M_{\text{FC}} - M_{\text{ZFC}})}{dT} \quad (2)$$

Real samples often exhibit a distribution of T_B , hence the average blocking temperature is conventionally defined as the temperature at which 50% of the sample is in the superparamagnetic regime.^{58,60} This corresponds to the temperature at which the integral of the $f(T)$ reaches 50% of its maximum value, that is, the temperature at which the $(M_{\text{FC}} - M_{\text{ZFC}})$ curve is reduced to half of its value at 5 K. Recently, de Almeida et al.⁶¹ have proposed a modified formulation

$$f^*(T) \propto -\frac{1}{T} \frac{d(M_{\text{FC}} - M_{\text{ZFC}})}{dT} \quad (3)$$

This formula uses an additional $1/T$ term, which aims to renormalize the contribution of the particles with the largest volume, which reverse at higher T_B , and due to their larger magnetic moment they could bias the distribution of blocking temperatures to larger values. The average T_B is now defined as the temperature at which the integral of the $f^*(T)$ reaches 50% of its maximum value (Figure 4c). In our analysis, we have considered both approaches, obtaining an average effective blocking temperature (T_B^*) of about 95 and 60 K, for the conventional and modified formulation, respectively. Both values are much larger than the 20 K measured for similar size particles.⁶² One could expect that such a large effective blocking temperature reflects the presence of a significant interparticle interacting regime. This hypothesis is supported

by the flat low-temperature part of the FC curve typical of strongly interacting particles.

To shed light on the possible scenario of interparticle interactions, we have analyzed the field dependence of the effective distribution of blocking temperature T_B^* calculated with both methods using the random anisotropy model (RAM) (Figure 4d). When the effect of magnetic interactions extends over a distance larger than the dimensions of individual particles, several of them can form a single magnetically correlated volume characterized by an effective anisotropy constant, resulting from the average of the individual particles. The field dependence of the blocking temperature reflects this behavior according to the formula

$$T_B(H) = \frac{K_6^{\pi}[D^3 + x(L_{\text{corr}}^3 - D^3)]}{6k_B \ln\left(\frac{\tau_m}{\tau_0}\right) \sqrt{1 + x \frac{(L_{\text{corr}}^3 - D^3)}{D^3}}} \left[1 - \frac{\mu_0 H M_S \sqrt{1 + x \frac{(L_{\text{corr}}^3 - D^3)}{D^3}}}{2K} \right]^{1.5} \quad (4)$$

where D is the individual particle diameter, L_{corr} is the average magnetic correlation length, x is the volume fraction of particles, K is the intrinsic anisotropy constant of the individual particles, and M_S is the saturation magnetization (see the [Supporting Information](#) for a more detailed derivation of the formula^{63–65}). Assuming that only the crystalline nanoparticles are responsible for the observed superparamagnetic relaxation, we have considered only the contribution of the crystalline nanoparticles in the RAM, fixing their saturation magnetization to the bulk value ($85 \text{ A m}^2 \text{ kg}^{-1}$), the average particle size to 3 nm, and the crystalline volume occupancy to 25%, according to the Rietveld refinement results. Despite limiting the model to the crystalline fraction only, fitting eq 4 to the data results in an accurate description of the experimental field dependence of T_B (Figure 4d), obtaining a first qualitative description of the magnetic organization inside the sample. Despite the different values, the fits to the two sets of T_B versus H data gave the same results, within the experimental error. The parameters of the fits suggest a correlated volume including an average of 8 NPs resulting from a correlation length of about 10 nm. Interestingly, the magnitude of the effective coupling is $1.5(1) \text{ pJ/m}$, at least 1 order of magnitude larger than what was observed for spinel ferrites with strong dipolar interactions.⁶⁵ Furthermore, the RAM suggests an intrinsic T_B for the individual particles of about 30(5) K, in good agreement with the experimental observations for cobalt ferrite particles of similar size.⁶² The fact that both methods give the same results is reasonable, considering that the RAM analyzes the field dependence trend, which is extremely similar for the two sets of data and not affected by the specific formulation of T_B . On the other hand, one can appreciate that the calculations result in an intrinsic anisotropy constant of about $510(20) \text{ kJ/m}^3$ versus $823(9) \text{ kJ/m}^3$ for the conventional and modified formulation, respectively. This discrepancy is connected to the different weights given to the contribution of the largest particles. As a result, the conventional and modified formulations somehow lead to the mode and median values of the anisotropy constant distribution, respectively.

The magnetization versus field curve measured at 5 K (Figure 5) shows a quite large coercive field $\mu_0 H_C \approx 1.4 \text{ T}$, even compared to ultrasmall crystalline cobalt ferrite nanoparticles exhibiting large surface anisotropy.⁶² The curve never

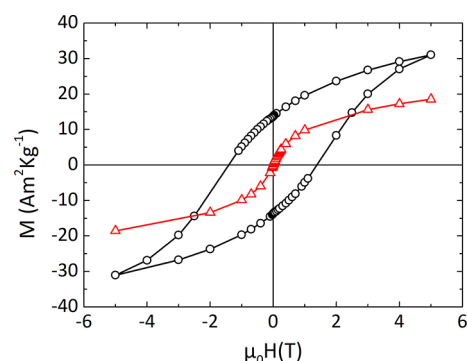


Figure 5. Magnetization versus field curve measured at 5 K (black circles) and 300 K (red triangles).

reaches full reversibility, even at 5 T, suggesting that the hysteresis is a minor loop. As a rough indication of the saturation magnetization, we have extrapolated its value applying the law of approach to saturation, obtaining $40 \text{ A m}^2 \text{ kg}^{-1}$. Since the crystalline phase represents only 25% of the total volume, even attributing to it the bulk value of saturation

magnetization ($85 \text{ A m}^2 \text{ kg}^{-1}$),⁶⁶ its amount is too small to reproduce the experimental value. An additional magnetization contribution (about $13 \text{ A m}^2 \text{ kg}^{-1}$ at 5 T) is needed from the major amorphous phase to match the experimentally measured value. The $M(H)$ curve recorded at 300 K (Figure 5) shows the typical superparamagnetic behavior of nanoparticles with no hysteretic behavior even if with a large susceptibility at high field responsible for a slow approach to saturation.

It is worth noting that we have also performed ΔM -plots measurements. Despite the protocol needs to fully saturate the sample in between the measurement steps and thus the results do not have absolute relevance, they still show a strong demagnetization effect on the remanent magnetization, connected to the presence of a strongly interacting regime⁶⁷ (see Supporting Information for further details).

Micromagnetic Model. To elucidate the complex structure of the system under investigation, we have developed a micromagnetic model by using the software Mumax3,⁶⁸ then used to reproduce the magnetization versus field curve measured at 5 K. To represent the large aggregates, we have created a simulation box of $96 \times 96 \times 96 \text{ nm}^3$, discretized in cubic cells of 3 nm edge. Besides, the sample was divided into

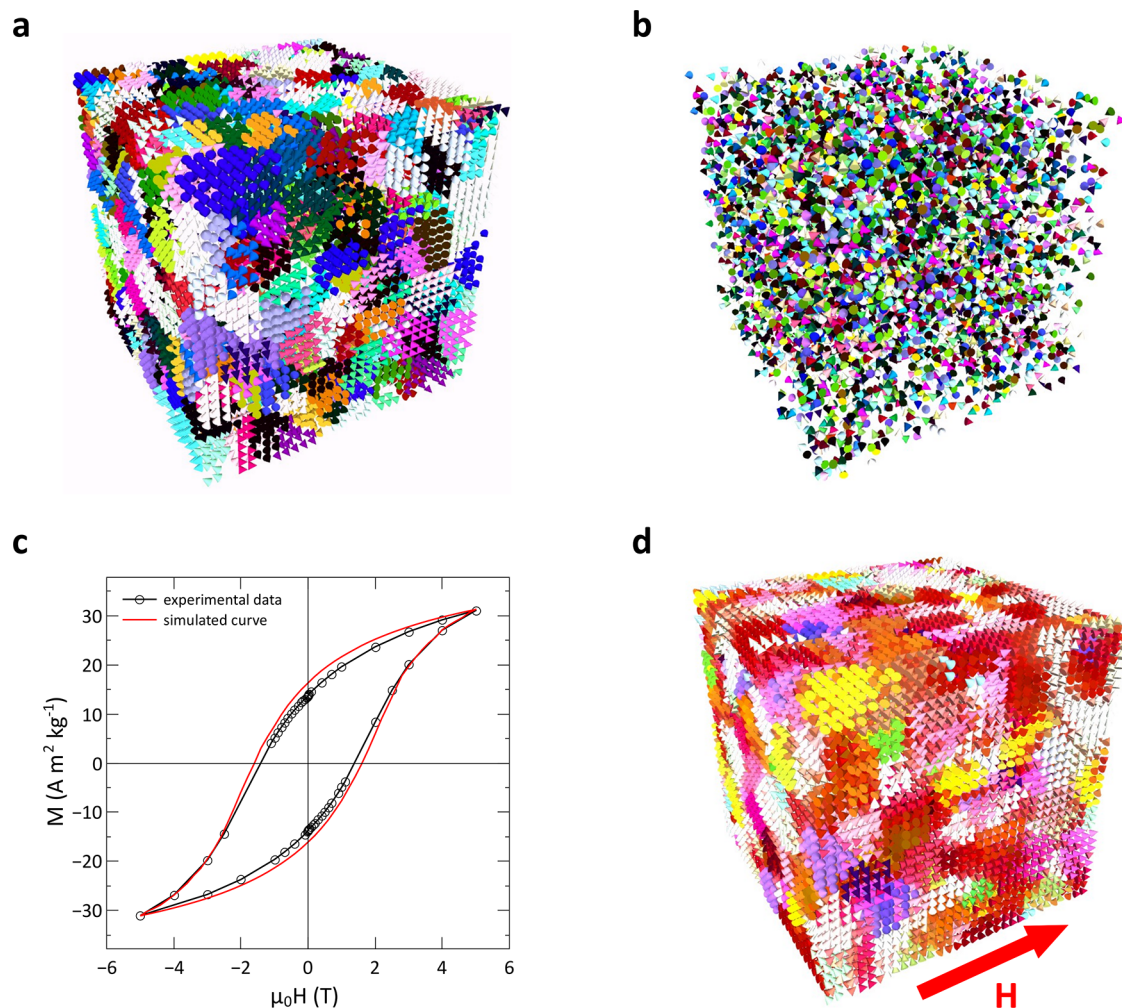


Figure 6. Micromagnetic model of the sample composed of individual crystalline cobalt ferrite nanoelements embedded in a granular amorphous matrix. For clarification, the matrix and the crystalline elements are shown individually in (a,b), respectively, with cones with different colors indicating the directions of the anisotropy easy axis. (c) The $M(H)$ curve obtained averaging over 10 different simulation seeds is compared to the experimental curve. (d) Even with an applied field of +5 T (direction indicated by the red arrow), the sample is not fully saturated (full saturation along the field direction indicated with red color).

10 nm grains by Voronoi tessellation, to reproduce the internal granular structure. Each grain owns an effective uniaxial anisotropy with a random orientation of easy axis, according to the RAM⁶⁹ (Figure 6a). Within each aggregate, 8192 cells have been used to individually reproduce the embedded 3 nm crystalline particles, corresponding to 25% of the total simulated volume, as estimated from the Rietveld refinement of the XRD pattern (Figure 6b). The simulated structure is repeated using periodic boundary conditions with 10 copies at each side of the original simulation box, for a total size for the virtual sample of about $2 \times 2 \times 2 \mu\text{m}^3$. To improve the statistical representation of the sample, the simulation was repeated 10 times with different random configurations, hence averaging the results.

The core–shell model for the magnetic structure of nanoparticles has a deep foundation in the literature.^{19–21} On the basis of this knowledge, we have extended this concept modeling our sample as crystalline core particles surrounded by a distorted surface phase that embeds them forming a continuous disordered matrix. As recently demonstrated, such disordered structure does not always represent a dead magnetic phase, but a magnetically canted structure, with low effective magnetization and very large magnetic anisotropy, coupled with the regular core structure.^{70,71} Hence, the crystalline elements have been defined as particles with bulklike cobalt ferrite properties,⁶⁶ that is, exchange stiffness of 12 pJ/m, saturation magnetization of $85 \text{ A m}^2 \text{ kg}^{-1}$, and cubic anisotropy of 290 KJ/m^3 with a random easy axis direction in each 3 nm element. Crosschecking the data emerging from the characterization of the sample, a solid and consistent model of the matrix has emerged. The $M(H)$ at 5 K reveals the presence of a large effective anisotropy which prevents the full saturation of the sample in the range of field $+5 \text{ T}/-5 \text{ T}$. Moreover, since the crystalline fraction accounts for only 25% of the volume, a large part of the moment should come from the amorphous fraction. On the other hand, Mössbauer data confirm that even with an externally applied field of 8 T, the sample shows a large canting angle of about 46° . To have a preliminar indication of the intrinsic saturation magnetization of the sample, we have used the value obtained from the law of approach to saturation. Since the $M(H)$ protocol does not fully saturate the sample, this approach cannot give values of absolute significance. Hence, the fit has been used only as an initial suggestion for a reasonable interval of confidence to guide the optimization of the saturation magnetization of the amorphous phase. Considering also the canting angle at 8 T and the relative experimental error, this range resulted in between ~ 40 and $60 \text{ A m}^2 \text{ kg}^{-1}$. Accordingly, the saturation magnetization of the amorphous matrix phase (M_s^{matrix}) was tuned in the range of ~ 30 – $50 \text{ A m}^2 \text{ kg}^{-1}$. Interestingly, despite the large magnetic anisotropy exhibited at low temperature at 300 K the $M(H)$ curve shows only the superparamagnetic contribution of the magnetic core, suggesting that the magnetic ordering of the matrix disappears below 300 K. On the basis of this, we have estimated the exchange stiffness of the matrix in 2 pJ/m. This is also in agreement with the strength of the coupling observed applying the RAM fitting procedure.

Within this framework, the only parameters to be optimized were the saturation magnetization of the amorphous phase and the effective magnetic anisotropy of the matrix grains. The best results (Figure 6c) have been obtained setting $M_s^{\text{matrix}} = 38 \text{ A m}^2 \text{ kg}^{-1}$ and using a log-normal distribution of magnetic

anisotropy values with a mean of 3.0 MJ/m^3 and standard deviation of 2.0 MJ/m^3 , resulting in a mode of 1.7 MJ/m^3 (Figure S8, Supporting Information). Furthermore, we have also verified that different ratios of crystalline/amorphous phase did not improve the simulations. It is worth mentioning that these values are in good agreement with what experimentally was observed for cobalt ferrite particles with surface distorted/canted structure, responsible for large effective magnetic anisotropy and reduced saturation magnetization for the entire particle.^{18,62,72–74} According to the model, the field used to measure the $M(H)$ loop allows the magnetization reversal of only a fraction of the matrix, responsible for the large coercive field measured. On the other hand, a large part of the sample gives an irreversible contribution and does not reach saturation, forming a large canting angle with the applied field (Figure 6d). As further validation of the model, we have simulated the system at 8 T (Figure S9, Supporting Information), obtaining an average canting angle of $40(2)^\circ$, in good agreement with the experimental Mössbauer data, and further reinforcing the validity of the micromagnetic model and the value of parameters used for the amorphous component.

In this micromagnetic model, the exchange coupling between different regions is simply calculated as the average between the two. Hence, the crystalline elements are integrated within the matrix grains with an effective exchange that is the average of the two values, reproducing a smooth transition between the two phases. To investigate the role of the coupling among each component, we have performed simulations individually removing each exchange contribution and dipolar interactions (Figure S10a, Supporting Information). Removing the exchange coupling among the matrix grains has minimal effects, with just a slight increment of coercivity. Indeed, the exchange interactions among amorphous grains with different easy axis directions tend to reduce the effective anisotropy and hence H_c . Removing independently the interactions among connected crystalline grains leads to the same effect since eventual small clusters of the low anisotropy crystalline elements would be more effective in reducing the effective anisotropy of the nanocomposite. A similar conclusion can be drawn when removing dipolar interactions, which own weak demagnetizing character. As expected, the main role is played by the exchange between crystalline and amorphous elements, which are strong enough to induce a single-phase behavior. In the absence of this exchange, a double phase magnetization reversal is strongly evident (Figure S10b, Supporting Information) with only a small fraction of the matrix reversing in the experimental range of applied field. The crystalline elements are not only embedded into the matrix but also solidly coupled to it. The hybrid crystalline–amorphous design is not based on perfect epitaxial interfaces, which are extremely sensitive to any defect. On the other hand, this design exploits the versatility of the homogeneous amorphous disorder that self-adjusts the interface structure to produce a smooth transition, which in turn allows for an extended range of coupling. Indeed this unique amorphous interface allows producing rigid exchange-coupled composites⁷⁵ and can preserve the coupling to an extremely long-range, reaching the micrometer scale in fully amorphous composites.²⁴ Within this context, the amorphous structure does not represent anymore a defective phase or an undesired product but can be seen as an integral element of the artificial nanostructure, where it reaches the quality of a very hard medium that cannot

be found in the parent crystalline material. It is worth remembering that this hybrid nanoarchitecture is obtained by just controlling the pH value of the coprecipitation synthesis process, allowing for a reduction in cost and complexity while obtaining an optimum high yield with no waste products, and maximized integration between the two components.

CONCLUSION

We have investigated the properties of an unconventional hybrid nanoarchitecture made of crystalline inclusions with relatively high saturation magnetization grown from a magnetically hard amorphous parent structure. By combining the information on the structure and the magnetic properties, we have built a micromagnetic model to fully explain the properties of the system and underline the benefits of this exotic design. The main disordered phase owns an amorphous structure that behaves similarly to typical canted shell structures widely reported in the literature, that is, with reduced magnetization but large magnetic anisotropy. However, here it represents the majority of the sample and not just a thin layer on top of a bulklike core particle, hence constituting a second hard magnetic phase. The optimized synthesis process induces a smooth and gradual transition from the amorphous to the crystalline phase typical of amorphous interfaces, preserving long-range interactions and allowing one to create a well-integrated hybrid nanoarchitecture that behaves as an artificial single-phase material with enhanced magnetic anisotropy, well above the values achievable by the individual components. The extremely low cost and minimal complexity of the synthesis process make this efficient design of large interest for technological applications, in particular considering the high yield of the process. Nevertheless, this hybrid nanoarchitecture can be easily extended to other materials improving their magnetic, electric, and optical properties, paving the way for the development of a new class of hybrid-structured nanomaterials.

ASSOCIATED CONTENT

Supporting Information

The Supporting Information is available free of charge at <https://pubs.acs.org/doi/10.1021/acs.jpcc.1c00797>.

XRD patterns and analysis of the nanocomposite (CoFe_2O_4 + amorphous) and the $\text{Co}_{0.25}\text{Fe}_{2.75}\text{O}_4$ sample; additional TEM images of the nanocomposite (CoFe_2O_4 + amorphous) sample; description of the Mössbauer spectroscopy measured at high applied field; extensive description of the random anisotropy model (RAM), with raw data used for the calculations; IRM, DCD, and ΔM -plots analysis; comparison of $M(H)$ curves measured at 5 K for the nanocomposite (CoFe_2O_4 + amorphous) and the $\text{Co}_{0.25}\text{Fe}_{2.75}\text{O}_4$ sample; detailed description of the micromagnetic model and performed simulations (PDF)

AUTHOR INFORMATION

Corresponding Author

Giuseppe Muscas – Department of Physics, University of Cagliari, I-09042 Monserrato (CA), Italy; orcid.org/0000-0001-7508-0752; Email: giuseppe.muscas@dsf.unica.it

Authors

Sawssen Slimani – Dipartimento di Chimica e Chimica Industriale, Università degli Studi di Genova, I-16146 Genova, Italy; Istituto di Struttura della Materia-CNR, 00015 Monterotondo Scalo (RM), Italy; Laboratoire de Physique Appliquée, Faculté des Sciences, Université de Sfax, 3000 Sfax, Tunisia

Giorgio Concas – Department of Physics, University of Cagliari, I-09042 Monserrato (CA), Italy; orcid.org/0000-0003-3422-1066

Francesco Congiu – Department of Physics, University of Cagliari, I-09042 Monserrato (CA), Italy

Gianni Barucca – Dipartimento di Scienze e Ingegneria della Materia, dell'Ambiente ed Urbanistica, Università Politecnica delle Marche, 60131 Ancona, Italy; orcid.org/0000-0002-7368-6264

Nader Yaacoub – IMMM, Université du Main, CNRS UMR-6283, Le Mans 72085, France

Alessandro Talone – Istituto di Struttura della Materia-CNR, 00015 Monterotondo Scalo (RM), Italy; Dipartimento di Scienze, Università degli Studi "Roma Tre", 00154 Roma, Italy

Mourad Smari – Laboratoire de Physique Appliquée, Faculté des Sciences, Université de Sfax, 3000 Sfax, Tunisia; orcid.org/0000-0003-0090-3296

Essebt Dhahri – Laboratoire de Physique Appliquée, Faculté des Sciences, Université de Sfax, 3000 Sfax, Tunisia

Davide Peddis – Dipartimento di Chimica e Chimica Industriale, Università degli Studi di Genova, I-16146 Genova, Italy; Istituto di Struttura della Materia-CNR, 00015 Monterotondo Scalo (RM), Italy; orcid.org/0000-0003-0810-8860

Complete contact information is available at: <https://pubs.acs.org/doi/10.1021/acs.jpcc.1c00797>

Notes

The authors declare no competing financial interest.

ACKNOWLEDGMENTS

G.M. acknowledges the financial support from the PON AIM program (Project AIM1809115 - Num. Attività 3 - Linea 2.1). C. G., F. C., and G. M. acknowledge the CeSAR (Centro Servizi d'Ateneo per la Ricerca) of the University of Cagliari (Italy) for the magnetometry experiments.

REFERENCES

- Peddis, D. Magnetic Properties of Spinel Ferrite Nanoparticles: Influence of the Magnetic Structure. In *Magnetic Nanoparticle Assemblies*; Trohidou, K. N., Ed.; Pan Stanford Publishing, 2014; Vol. 7, pp 159–198.
- Roca, A. G.; Costo, R.; Rebolledo, A. F.; Veintemillas-Verdaguer, S.; Tartaj, P.; González-Carreño, T.; Morales, M. P.; Serna, C. J. Progress in the Preparation of Magnetic Nanoparticles for Applications in Biomedicine. *J. Phys. D: Appl. Phys.* **2009**, 42 (22), 224002.
- Haun, J. B.; Yoon, T.-J.; Lee, H.; Weissleder, R. Magnetic Nanoparticle Biosensors. *Wiley Interdiscip. Rev. Nanomedicine Nanobiotechnology* **2010**, 2 (3), 291–304.
- Schultz-Sikma, E. a; Joshi, H. M.; Ma, Q.; MacRenaris, K. W.; Eckermann, A. L.; Dravid, V. P.; Meade, T. J. Probing the Chemical Stability of Mixed Ferrites: Implications for Magnetic Resonance Contrast Agent Design. *Chem. Mater.* **2011**, 23 (10), 2657–2664.
- Lartigue, L.; Hugounenq, P.; Alloyeau, D.; Clarke, S. P.; Lévy, M.; Bacri, J.-C.; Bazzi, R.; Brougham, D. F.; Wilhelm, C.; Gazeau, F.

Cooperative Organization in Iron Oxide Multi-Core Nanoparticles Potentiates Their Efficiency as Heating Mediators and MRI Contrast Agents. *ACS Nano* **2012**, *6* (12), 10935–10949.

(6) Guardia, P.; Pérez, N.; Labarta, A.; Batlle, X. Controlled Synthesis of Iron Oxide Nanoparticles over a Wide Size Range. *Langmuir* **2010**, *26* (8), 5843–5847.

(7) Thorat, N. D.; Khot, V. M.; Salunkhe, A. B.; Prasad, A. I.; Ningthoujam, R. S.; Pawar, S. H. Surface Functionalized LSMO Nanoparticles with Improved Colloidal Stability for Hyperthermia Applications. *J. Phys. D: Appl. Phys.* **2013**, *46* (10), 105003.

(8) Hugounenq, P.; Levy, M.; Alloyeau, D.; Lartigue, L.; Dubois, E.; Cabuil, V.; Ricolleau, C.; Roux, S.; Wilhelm, C.; Gazeau, F.; Bazzi, R. Iron Oxide Monocrystalline Nanoflowers for Highly Efficient Magnetic Hyperthermia. *J. Phys. Chem. C* **2012**, *116* (29), 15702–15712.

(9) Sakellari, D.; Brintakis, K.; Kostopoulou, A.; Myrovali, E.; Simeonidis, K.; Lappas, A.; Angelakeris, M. Ferrimagnetic Nanocrystal Assemblies as Versatile Magnetic Particle Hyperthermia Mediators. *Mater. Sci. Eng., C* **2016**, *58*, 187–193.

(10) Bender, P.; Fock, J.; Frandsen, C.; Hansen, M. F.; Balceris, C.; Ludwig, F.; Posth, O.; Wetterskog, E.; Bogart, L. K.; Southern, P.; Szczerba, W.; Zeng, L.; Witte, K.; Grüttner, C.; Westphal, F.; Honecker, D.; González-Alonso, D.; Fernández Barquín, L.; Johansson, C. Relating Magnetic Properties and High Hyperthermia Performance of Iron Oxide Nanoflowers. *J. Phys. Chem. C* **2018**, *122* (5), 3068–3077.

(11) Raj, K.; Moskowitz, B.; Casciari, R. Advances in Ferrofluid Technology. *J. Magn. Magn. Mater.* **1995**, *149* (1–2), 174–180.

(12) Kainz, Q. M.; Reiser, O. Polymer- and Dendrimer-Coated Magnetic Nanoparticles as Versatile Supports for Catalysts, Scavengers, and Reagents. *Acc. Chem. Res.* **2014**, *47* (2), 667–677.

(13) Srivatsan, T.; Nanomaterials, S.; Edelstein, A. S.; Cammarata, R. C. Synthesis, Properties, and Applications. *Mater. Manuf. Processes* **2012**, *27* (10), 1145–1145.

(14) Skomski, R.; Manchanda, P.; Kumar, P. K.; Balamurugan, B.; Kashyap, A.; Sellmyer, D. J. Predicting the Future of Permanent-Magnet Materials. *IEEE Trans. Magn.* **2013**, *49* (7), 3215–3220.

(15) Zhao, W.; Liu, Z.; Sun, Z.; Zhang, Q.; Wei, P.; Mu, X.; Zhou, H.; Li, C.; Ma, S.; He, D.; Ji, P.; Zhu, W.; Nie, X.; Su, X.; Tang, X.; Shen, B.; Dong, X.; Yang, J.; Liu, Y.; Shi, J. Superparamagnetic Enhancement of Thermoelectric Performance. *Nature* **2017**, *549* (7671), 247–251.

(16) Zhao, W.; Liu, Z.; Wei, P.; Zhang, Q.; Zhu, W.; Su, X.; Tang, X.; Yang, J.; Liu, Y.; Shi, J.; Chao, Y.; Lin, S.; Pei, Y. Magnetoelectric Interaction and Transport Behaviours in Magnetic Nanocomposite Thermoelectric Materials. *Nat. Nanotechnol.* **2017**, *12* (1), 55–60.

(17) Vasilakaki, M.; Chikina, I.; Shikin, V. B.; Ntallis, N.; Peddis, D.; Varlamov, A. A.; Trohidou, K. N. Towards High-Performance Electrochemical Thermal Energy Harvester Based on Ferrofluids. *Appl. Mater. Today* **2020**, *19*, 100587.

(18) Vázquez-Vázquez, C.; López-Quintela, M. a.; Buján-Núñez, M. C.; Rivas, J. Finite Size and Surface Effects on the Magnetic Properties of Cobalt Ferrite Nanoparticles. *J. Nanopart. Res.* **2011**, *13* (4), 1663–1676.

(19) Kodama, R. H.; Berkowitz, A. E.; McNiff, E. J., Jr.; Foner, S. Surface Spin Disorder in NiFe₂O₄ Nanoparticles. *Phys. Rev. Lett.* **1996**, *77* (2), 394–397.

(20) Morales, M. P.; Serna, C. J.; Bødker, F.; Mørup, S. Spin Canting Due to Structural Disorder in Maghemite. *J. Phys.: Condens. Matter* **1997**, *9* (25), 5461–5467.

(21) Krycka, K. L.; Booth, R. A.; Hogg, C. R.; Ijiri, Y.; Borchers, J. A.; Chen, W. C.; Watson, S. M.; Laver, M.; Gentile, T. R.; Dedon, L. R.; Harris, S.; Rhyne, J. J.; Majetich, S. A. Core-Shell Magnetic Morphology of Structurally Uniform Magnetite Nanoparticles. *Phys. Rev. Lett.* **2010**, *104* (20), 207203.

(22) López-Ortega, A.; Estrader, M.; Salazar-Alvarez, G.; Roca, A. G.; Nogués, J. Applications of Exchange Coupled Bi-Magnetic Hard/Soft and Soft/Hard Magnetic Core/Shell Nanoparticles. *Phys. Rep.* **2015**, *553* (0), 1–32.

(23) Beyerlein, I. J.; Demkowicz, M. J.; Misra, A.; Ueberuaga, B. P. Defect-Interface Interactions. *Prog. Mater. Sci.* **2015**, *74*, 125–210.

(24) Muscas, G.; Brucas, R.; Jönsson, P. E. Bringing Nanomagnetism to the Mesoscale with Artificial Amorphous Structures. *Phys. Rev. B: Condens. Matter Mater. Phys.* **2018**, *97* (17), 174409.

(25) Lak, A.; Disch, S.; Bender, P. Embracing Defects and Disorder in Magnetic Nanoparticles. *Adv. Sci.* **2021**, *8*, 2002682.

(26) Lappas, A.; Antonopoulos, G.; Brintakis, K.; Vasilakaki, M.; Trohidou, K. N.; Iannotti, V.; Ausanio, G.; Kostopoulou, A.; Abeykoon, M.; Robinson, I. K.; Bozin, E. S. Vacancy-Driven Noncubic Local Structure and Magnetic Anisotropy Tailoring in Fe₃O₄-Fe₃-δ O₄ Nanocrystals. *Phys. Rev. X* **2019**, *9* (4), 41044.

(27) Muscas, G.; Yaacoub, N.; Concas, G.; Sayed, F.; Sayed Hassan, R.; Greneche, J. M.; Cannas, C.; Musinu, A.; Foglietti, V.; Casciardi, S.; Sangregorio, C.; Peddis, D. Evolution of the Magnetic Structure with Chemical Composition in Spinel Iron Oxide Nanoparticles. *Nanoscale* **2015**, *7* (32), 13576–13585.

(28) Sanna Angotzi, M.; Mameli, V.; Cara, C.; Musinu, A.; Sangregorio, C.; Niznansky, D.; Xin, H. L.; Vejpravova, J.; Cannas, C. Coupled Hard-Soft Spinel Ferrite-Based Core-Shell Nanoarchitectures: Magnetic Properties and Heating Abilities. *Nanoscale Adv.* **2020**, *2* (8), 3191–3201.

(29) Lavorato, G. C.; Lima, E.; Troiani, H. E.; Zysler, R. D.; Winkler, E. L. Tuning the Coercivity and Exchange Bias by Controlling the Interface Coupling in Bimagnetic Core/Shell Nanoparticles. *Nanoscale* **2017**, *9* (29), 10240–10247.

(30) Sánchez, E. H.; Vasilakaki, M.; Lee, S. S.; Normile, P. S.; Muscas, G.; Murgia, M.; Andersson, M. S.; Singh, G.; Mathieu, R.; Nordblad, P.; Ricci, P. C.; Peddis, D.; Trohidou, K. N.; Nogués, J.; De Toro, J. A. Simultaneous Individual and Dipolar Collective Properties in Binary Assemblies of Magnetic Nanoparticles. *Chem. Mater.* **2020**, *32* (3), 969–981.

(31) Wu, Z.; Liu, J.; Li, Y.; Cheng, Z.; Li, T.; Zhang, H.; Lu, Z.; Yang, B. Self-Assembly of Nanoclusters into Mono-, Few-, and Multilayered Sheets via Dipole-Induced Asymmetric van Der Waals Attraction. *ACS Nano* **2015**, *9* (6), 6315–6323.

(32) Shi, W.; Song, S.; Zhang, H. Hydrothermal Synthetic Strategies of Inorganic Semiconducting Nanostructures. *Chem. Soc. Rev.* **2013**, *42* (13), 5714.

(33) Branda, F. The Sol-Gel Route to Nanocomposites. In *Advances in Nanocomposites - Synthesis, Characterization and Industrial Applications*; Reddy, B., Ed.; InTech, 2011.

(34) Lok, M. Coprecipitation. In *Synthesis of Solid Catalysts*; de Jong, K. P., Ed.; Wiley-VCH Verlag GmbH & Co. KGaA: Weinheim, Germany, 2009; pp 135–151.

(35) Dixit, S.; Jeevanandam, P. Synthesis of Iron Oxide Nanoparticles by Thermal Decomposition Approach. *Adv. Mater. Res.* **2009**, *67*, 221–226.

(36) Okoli, C.; Sanchez-Dominguez, M.; Boutonnet, M.; Järås, S.; Civera, C.; Solans, C.; Kuttuva, G. R. Comparison and Functionalization Study of Microemulsion-Prepared Magnetic Iron Oxide Nanoparticles. *Langmuir* **2012**, *28* (22), 8479–8485.

(37) Mascolo, M.; Pei, Y.; Ring, T. Room Temperature Co-Precipitation Synthesis of Magnetite Nanoparticles in a Large PH Window with Different Bases. *Materials* **2013**, *6* (12), 5549–5567.

(38) Massart, R. Preparation of Aqueous Magnetic Liquids in Alkaline and Acidic Media. *IEEE Trans. Magn.* **1981**, *17* (2), 1247–1248.

(39) Stein, C. R.; Bezerra, M. T. S.; Holanda, G. H. A.; André-Filho, J.; Morais, P. C. Structural and Magnetic Properties of Cobalt Ferrite Nanoparticles Synthesized by Co-Precipitation at Increasing Temperatures. *AIP Adv.* **2018**, *8* (5), No. 056303.

(40) Gandhi, S.; Issar, S.; Mahapatra, A. K.; Roy, I. Cobalt Ferrite Nanoparticles for Bimodal Hyperthermia and Their Mechanistic Interactions with Lysozyme. *J. Mol. Liq.* **2020**, *310*, 113194.

(41) Blesa, M. A.; Matijević, E. Phase Transformations of Iron Oxides, Oxohydroxides, and Hydrated Oxides in Aqueous Media. *Adv. Colloid Interface Sci.* **1989**, *29* (3–4), 173–221.

- (42) Sugawara, E.; Nikaido, H. Properties of AdeABC and AdeIJK Efflux Systems of *Acinetobacter Baumannii* Compared with Those of the AcrAB-TolC System of *Escherichia Coli*. *Antimicrob. Agents Chemother.* **2014**, *58* (12), 7250–7257.
- (43) Shirsath, S. E.; Mane, M. L.; Yasukawa, Y.; Liu, X.; Morisako, A. Chemical Tuning of Structure Formation and Combustion Process in CoDy_{0.1}Fe_{1.9}O₄ Nanoparticles: Influence@pH. *J. Nanopart. Res.* **2013**, *15* (10), 1976.
- (44) Zhao, D.; Wu, X.; Guan, H.; Han, E. Study on Supercritical Hydrothermal Synthesis of CoFe₂O₄ Nanoparticles. *J. Supercrit. Fluids* **2007**, *42* (2), 226–233.
- (45) Jolivet, J.-P.; Cassaignon, S.; Chanéac, C.; Chiche, D.; Tronc, E. Design of Oxide Nanoparticles by Aqueous Chemistry. *J. Sol-Gel Sci. Technol.* **2008**, *46* (3), 299–305.
- (46) Schneider, C. A.; Rasband, W. S.; Eliceiri, K. W. NIH Image to ImageJ: 25 Years of Image Analysis. *Nat. Methods* **2012**, *9* (7), 671–675.
- (47) Morrish, A. H. *The Physical Principles of Magnetism*; IEEE: New York, 2001.
- (48) Fernandes de Medeiros, I. A.; Lopes-Moriyama, A. L.; de Souza, C. P. Effect of Synthesis Parameters on the Size of Cobalt Ferrite Crystallite. *Ceram. Int.* **2017**, *43* (5), 3962–3969.
- (49) Lutterotti, L.; Matthies, S.; Wenk, H. R. MAUD: A Friendly Java Program for Material Analysis Using Diffraction. *IUCr Newsl. CPD* **1999**, No. 21, pp 14–15.
- (50) Palomares Sánchez, S. A.; Ponce-Castañeda, S.; Martínez, J. R.; Ruiz, F.; Chumakov, Y.; Domínguez, O. Quantitative Analysis of Iron Oxide Particles Embedded in an Amorphous Xerogel Matrix. *J. Non-Cryst. Solids* **2003**, *325* (1–3), 251–257.
- (51) Greenwood, N. N.; Gibb, T. C. *Mössbauer Spectroscopy*; Yoshida, Y., Langouche, G., Ed.; Springer Netherlands: Dordrecht, 1971.
- (52) Bancroft, G. M. *Mössbauer Spectroscopy: An Introduction for Inorganic Chemists and Geochemists*; McGraw-Hill: London, 1973.
- (53) Mørup, S.; Dumesic, J. A.; Topsøe, E. Magnetic Microcrystals. In *Applications of Mössbauer Spectroscopy*; Cohen, R. L., Ed.; Elsevier: New York, 1980; pp 1–53; DOI: 10.1016/B978-0-12-178402-7.50007-5.
- (54) Tronc, E.; Prené, P.; Jolivet, J. P.; Dormann, J. L.; Grenèche, J. M. Spin Canting in γ -Fe₂O₃ Nanoparticles. *Hyperfine Interact.* **1998**, *112* (1), 97–100.
- (55) Coey, J. M. D. Noncollinear Spin Arrangement in Ultrafine Ferrimagnetic Crystallites. *Phys. Rev. Lett.* **1971**, *27* (17), 1140–1142.
- (56) Peddis, D.; Yaacoub, N.; Ferretti, M.; Martinelli, A.; Piccaluga, G.; Musinu, A.; Cannas, C.; Navarra, G.; Greneche, J. M.; Fiorani, D. Cationic Distribution and Spin Canting in CoFe₂O₄ Nanoparticles. *J. Phys.: Condens. Matter* **2011**, *23* (42), 426004.
- (57) Gittleman, J. I.; Abeles, B.; Bozowski, S. Superparamagnetism and Relaxation Effects in Granular Ni-SiO₂ and Ni-Al₂O₃ Films. *Phys. Rev. B* **1974**, *9* (9), 3891–3897.
- (58) Bruvera, I. J.; Mendoza Zélis, P.; Pilar Calatayud, M.; Goya, G. F.; Sánchez, F. H. Determination of the Blocking Temperature of Magnetic Nanoparticles: The Good, the Bad, and the Ugly. *J. Appl. Phys.* **2015**, *118* (18), 184304.
- (59) Concas, G.; Congiu, F.; Muscas, G.; Peddis, D. Determination of Blocking Temperature in Magnetization and Mössbauer Time Scale: A Functional Form Approach. *J. Phys. Chem. C* **2017**, *121* (30), 16541–16548.
- (60) Mamiya, H.; Ohnuma, M.; Nakatani, I.; Furubayashim, T. Extraction of Blocking Temperature Distribution from Zero-Field-Cooled and Field-Cooled Magnetization Curves. *IEEE Trans. Magn.* **2005**, *41* (10), 3394–3396.
- (61) de Almeida, A. A.; De Biasi, E.; Mansilla, M. V.; Valdés, D. P.; Troiani, H. E.; Urretavizcaya, G.; Torres, T. E.; Rodríguez, L. M.; Fregenal, D. E.; Bernardi, G. C.; Winkler, E. L.; Goya, G. F.; Zysler, R. D.; Lima, E. Magnetic Hyperthermia Experiments with Magnetic Nanoparticles in Clarified Butter Oil and Paraffin: A Thermodynamic Analysis. *J. Phys. Chem. C* **2020**, *124* (50), 27709–27721.
- (62) Peddis, D.; Mansilla, M. V.; Mørup, S.; Cannas, C.; Musinu, A.; Piccaluga, G.; D'Orazio, F.; Lucari, F.; Fiorani, D.; D'Orazio, F. Spin-Canting and Magnetic Anisotropy in Ultrasmall CoFe₂O₄ Nanoparticles. *J. Phys. Chem. B* **2008**, *112* (29), 8507–8513.
- (63) Weissmüller, J.; Michels, A.; Barker, J. G.; Wiedenmann, A.; Erb, U.; Shull, R. D. Analysis of the Small-Angle Neutron Scattering of Nanocrystalline Ferromagnets Using a Micromagnetics Model. *Phys. Rev. B: Condens. Matter Mater. Phys.* **2001**, *63* (21), 214414.
- (64) Michels, a.; Viswanath, R.; Barker, J.; Birringer, R.; Weissmüller, J. Range of Magnetic Correlations in Nanocrystalline Soft Magnets. *Phys. Rev. Lett.* **2003**, *91* (26), 267204.
- (65) Muscas, G.; Concas, G.; Laureti, S.; Testa, A. M.; Mathieu, R.; De Toro, J. A.; Cannas, C.; Musinu, A.; Novak, M. A.; Sangregorio, C.; Lee, S. S.; Peddis, D. The Interplay between Single Particle Anisotropy and Interparticle Interactions in Ensembles of Magnetic Nanoparticles. *Phys. Chem. Chem. Phys.* **2018**, *20* (45), 28634–28643.
- (66) Coey, J. M. D. *Magnetism and Magnetic Materials*; Cambridge University Press, 2001.
- (67) De Toro, J. A.; Vasilakaki, M.; Lee, S. S.; Andersson, M. S.; Normile, P. S.; Yaacoub, N.; Murray, P.; Sánchez, E. H.; Muñoz, P.; Peddis, D.; Mathieu, R.; Liu, K.; Geshev, J.; Trohidou, K. N.; Nogués, J. Remanence Plots as a Probe of Spin Disorder in Magnetic Nanoparticles. *Chem. Mater.* **2017**, *29* (19), 8258–8268.
- (68) Vansteenkiste, A.; Leliaert, J.; Dvornik, M.; Helsen, M.; Garcia-Sanchez, F.; Van Waeyenberge, B. The Design and Verification of MuMax3. *AIP Adv.* **2014**, *4* (10), 107133.
- (69) Herzer, G. The Random Anisotropy Model - A Critical Review and Update. In *Properties and Applications of Nanocrystalline Alloys from Amorphous Precursors*; Idzikowski, B., Svec, P., Miglierini, M., Eds.; NATO Science Series; Springer Netherlands: Berlin/Heidelberg, 2005; Vol. 184, pp 15–34.
- (70) Krycka, K. L.; Borchers, J. A.; Booth, R. A.; Ijiri, Y.; Hasz, K.; Rhyne, J. J.; Majetich, S. A. Origin of Surface Canting within Fe₃O₄ Nanoparticles. *Phys. Rev. Lett.* **2014**, *113* (14), 147203.
- (71) Zákutná, D.; Nižňanský, D.; Barnsley, L. C.; Babcock, E.; Salhi, Z.; Feoktystov, A.; Honecker, D.; Disch, S. Field Dependence of Magnetic Disorder in Nanoparticles. *Phys. Rev. X* **2020**, *10* (3), No. 031019.
- (72) Topkaya, R.; Akman, Ö.; Kazan, S.; Aktaş, B.; Durmus, Z.; Baykal, A. Surface Spin Disorder and Spin-Glass-like Behaviour in Manganese-Substituted Cobalt Ferrite Nanoparticles. *J. Nanopart. Res.* **2012**, *14* (10), 1156.
- (73) Hu, L.; de Montferrand, C.; Lalatonne, Y.; Motte, L.; Brioude, A. Effect of Cobalt Doping Concentration on the Crystalline Structure and Magnetic Properties of Monodisperse Co_xFe_{3-x}O₄ Nanoparticles within Nonpolar and Aqueous Solvents. *J. Phys. Chem. C* **2012**, *116* (7), 4349–4355.
- (74) Song, Q.; Zhang, Z. J. Controlled Synthesis and Magnetic Properties of Bimagnetic Spinel Ferrite CoFe₂O₄ and MnFe₂O₄ Nanocrystals with Core–Shell Architecture. *J. Am. Chem. Soc.* **2012**, *134* (24), 10182–10190.
- (75) Rani, P.; Muscas, G.; Stopfel, H.; Andersson, G.; Jönsson, P. E. Rigid Exchange Coupling in Rare-Earth-Lean Amorphous Hard/Soft Nanocomposites. *Adv. Electron. Mater.* **2020**, *6* (11), 2000573.